arXiv:1608.02852v1 [astro-ph.SR] 9 Aug 2016

Spectra and rates of bremsstrahlung neutrino emission in stars

Gang Guo[1] and Yong-Zhong Qian[2,1,*]

[1] *Center for Nuclear Astrophysics, Department of Physics and Astronomy, Shanghai Jiao Tong University, Shanghai 200240, China*

[2] *School of Physics and Astronomy, University of Minnesota, Minneapolis, MN 55455, USA*

(Dated: August 10, 2016)

Abstract

We calculate the energy-differential rate for neutrino emission from electron-nucleus bremsstrahlung in stellar interiors taking into account the effects of electron screening and ionic correlations. We compare the energy-differential and the net rates, as well as the average $\bar{\nu}_e$ and $\bar{\nu}_x$ ($x = \mu, \tau$) energies, for this process with those for $e^{\pm}$ pair annihilation, plasmon decay, and photo-neutrino emission over a wide range of temperature and density. We also compare our updated energy loss rates for the above thermal neutrino emission processes with the fitting formulas widely used in stellar evolution models and determine the temperature and density domain in which each process dominates. We discuss the implications of our results for detection of $\bar{\nu}_e$ from massive stars during their pre-supernova evolution and find that pair annihilation makes the predominant contribution to the signal from the thermal emission processes.

PACS numbers: 95.30.Cq, 52.27.Aj, 12.15.Ji, 95.85.Ry

* qian@physics.umn.edu

I. INTRODUCTION

Stars are profuse sources of neutrinos. A prominent example is the solar neutrinos produced by weak nuclear reactions including electron capture and β decay. For stars like the sun and those of higher masses, as temperature and density increase during later stages of their evolution, $\nu\bar{\nu}$ pair production by $e^{\pm}$ pair annihilation, plasmon decay, photo-neutrino emission, and electron-nucleus bremsstrahlung becomes more and more important. Indeed, for those stars that can ignite core carbon (C) burning, the energy loss subsequent to C ignition is dominated by the above so-called thermal neutrino emission processes. For stars of $\gtrsim 8\,M_{\odot}$ ($M_{\odot}$ being the mass of the sun), neutrinos not only drive their evolution by cooling their interiors but also play dynamic roles in their core collapse and the ensuing supernova explosion.

The thermal neutrino emission processes in stellar interiors have been studied extensively [1–11]. As neutrinos free-stream out of massive stars during their pre-supernova evolution, the pertinent quantity for stellar evolution is the energy loss rate of each process. Practically, fitting formulas for these rates given by Ref. [10] have been widely used in stellar evolution models. As thermal neutrino emission depends on temperature and density and evolves as stars age, these neutrinos would constitute a unique probe of the conditions in stellar interiors, thereby providing a potential test of stellar evolution models [12–15]. Even if there might not be sufficient statistics to probe the details of stellar evolution, unambiguous detection of pre-supernova neutrinos from a nearby massive star would at least provide advance warning for the subsequent supernova explosion [15–17]. For the above purposes, it is important to calculate the detailed spectra of the thermal neutrino emission processes. In addition, neutrino signals from massive stars during their pre-supernova evolution are affected by flavor transformation through the Mikheyev-Smirnov-Wolfenstein (MSW) mechanism [18, 19]. A careful analysis of the MSW effect on these neutrino signals also requires knowledge of the neutrino spectra.

The neutrino spectra for the thermal emission processes can be obtained from the corresponding energy-differential rates. Previous works [13, 16, 20–24] have studied the neutrino spectra for $e^{\pm}$ pair annihilation, plasmon decay, and photo-neutrino emission. The spectra for electron-nucleus bremsstrahlung have not received as much attention. In particular, we are not aware of a detailed comparison of the spectra for this and other thermal emission

processes. In this paper we focus on neutrino emission from electron-nucleus bremsstrahlung in massive stars and its importance relative to other processes. Following a detailed comparison of the energy-differential rates of all the thermal neutrino emission processes during the pre-supernova evolution of a massive star, we find that $e^{\pm}$ pair annihilation makes the predominant contribution to the $\bar{\nu}_e$ signal from these processes for detection through capture on protons.

We present a detailed derivation of the energy-differential rate for neutrino emission from electron-nucleus bremsstrahlung in Sec. II. We compare the energy-differential and the net rates, as well as the average $\bar{\nu}_e$ and $\bar{\nu}_x$ ($x = \mu, \tau$) energies, for this and other thermal neutrino emission processes over a wide range of temperature and density in Sec. III. We also compare our updated energy loss rates for individual thermal neutrino emission processes with the fitting formulas of Ref. [10] and determine the temperature and density domain in which each process dominates in Sec. IV. We discuss the implications of our results for detection of $\bar{\nu}_e$ from massive stars during their pre-supernova evolution and give conclusions in Sec. V.

II. ENERGY-DIFFERENTIAL RATES FOR BREMSSTRAHLUNG NEUTRINO EMISSION

Neutrino emission from electron-nucleus bremsstrahlung is denoted by

$$(Z, A) + e^- \rightarrow (Z, A) + e^- + \nu_\alpha + \bar{\nu}_\alpha, \tag{1}$$

where (Z, A) represents a nucleus of proton number Z and mass number A, and $\alpha = e, x$. As shown in Fig. 1, the leading-order Feynman diagrams for this process are very similar to those for photo-neutrino emission, except that the photon here is linked to the nucleus and thus is off-shell (virtual). Both charged-current (CC, W-exchange) and neutral-current (NC, Z^0-exchange) interactions contribute to $\nu_e\bar{\nu}_e$ pair production, while only NC interactions contribute to $\nu_x\bar{\nu}_x$ pair production.

In the hot and dense stellar interior, medium effects should be taken into account for thermal processes. For electron-nucleus bremsstrahlung, an important effect is electron screening that modifies the Coulomb interaction between the electron and the nucleus. The effective screened potential for a single nucleus (Z, A) can be written in the momentum

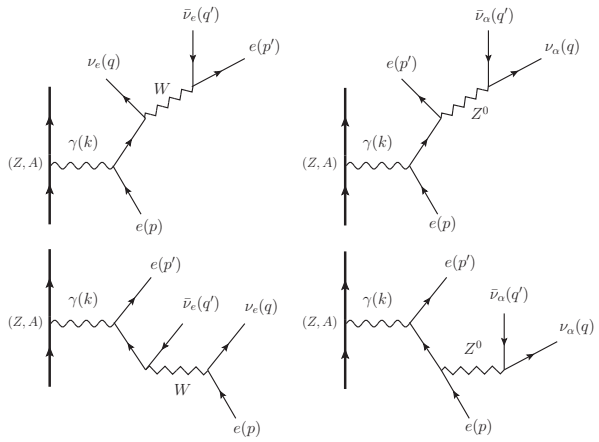

FIG. 1. Leading-order Feynman diagrams for neutrino emission from electron-nucleus bremsstrahlung.

space as

$$V_{\rm eff}(|\mathbf{k}|) = \frac{Zef(|\mathbf{k}|)}{\mathbf{k}^2\epsilon(|\mathbf{k}|)}, \tag{2}$$

where $\mathbf{k}$ is the momentum transfer to the electron, e is the magnitude of the electron charge, and $\epsilon(|\mathbf{k}|)$ is the static dielectric function that accounts for electron screening. In Eq. (2),

$$f(|\mathbf{k}|) = \frac{3[\sin(|\mathbf{k}|r_c) - (|\mathbf{k}|r_c)\cos(|\mathbf{k}|r_c)]}{(|\mathbf{k}|r_c)^3} \tag{3}$$

is the form factor corresponding to a uniform charge distribution within the charge radius r_c for the nucleus (Z, A). We consider $\rho < 4.3 \times 10^{11}$ g cm^{-3}, for which medium effects on the charge distribution within a nucleus can be ignored, and take $r_c = 1.15A^{1/3}$ fm. In general, the effective potential in Eq. (2) cannot be simply applied to all nuclei in the medium. This is because ionic correlations can be important and a structure factor $S_\Gamma(|\mathbf{k}|)$ is required to account for these. Below we discuss $\epsilon(|\mathbf{k}|)$ and $S_\Gamma(|\mathbf{k}|)$ in some detail, and then derive the matrix elements and the energy-differential rates for neutrino emission from electron-nucleus bremsstrahlung. Throughout the paper, we use the natural units where the reduced Planck constant $\hbar$ and the speed of light c are set to unity.

A. Static dielectric function $\epsilon(|\mathbf{k}|)$

The hot and dense stellar matter is composed of $e^\pm$ in a background of positive ions. For the conditions of interest, these ions are simply the bare nuclei. As $e^\pm$ are much lighter and

thus more mobile than ions, screening of the electron-nucleus Coulomb interaction is caused by $e^{\pm}$. To a good approximation, we can assume that ions are fixed and discuss how a static electric field is screened by $e^{\pm}$. We first calculate the screening effect by generalizing the semiclassical approximation used in Ref. [25] to include both e^- and e^+.

In an ideal gas, the equilibrium $e^{\pm}$ number densities are

$$n_{e^{\pm}} = \frac{2}{(2\pi)^3}\int_0^\infty N_{\pm}(E)d^3\mathbf{p} \equiv \frac{1}{4\pi^3}\int_0^\infty \frac{d^3\mathbf{p}}{\exp[(E\pm\mu)/(k_BT)]+1}, \tag{4}$$

where $N_{\pm}(E)$ are the $e^{\pm}$ occupation numbers at energy E, $\mathbf{p}$ is the corresponding momentum, μ is the chemical potential, k_B is the Boltzmann constant, and T is the temperature. For a specific T, μ can be obtained from the net electron number density $n_e \equiv n_{e^-} - n_{e^+} = \rho/(\mu_e m_u)$, where ρ is the mass density of nuclei associated with the $e^{\pm}$ gas, m_u is the atomic mass unit, and μ_e is the molecular weight per net electron. For the simple case of a neutral uniform one-component plasma (OCP), $\mu_e = A/Z$. When a nucleus (Z, A) is introduced into this OCP, its screened potential $\phi(r)$ shifts the equilibrium $e^{\pm}$ number densities at a distance r to

$$n'_{e^{\pm}}(r) = \frac{1}{4\pi^3}\int_0^\infty \frac{d^3\mathbf{p}}{\exp[(E\pm e\phi(r)\pm\mu)/(k_BT)]+1}. \tag{5}$$

Relative to the initial uniform OCP, the changes in the $e^{\pm}$ number densities to the leading order are

$$\delta n_{e^{\pm}}(r) \equiv n'_{e^{\pm}}(r) - n_{e^{\pm}} \approx \mp\frac{e\phi(r)}{4\pi^3 k_BT}\int_0^\infty \frac{\exp[(E\pm\mu)/(k_BT)]d^3\mathbf{p}}{\{\exp[(E\pm\mu)/(k_BT)]+1\}^2}. \tag{6}$$

According to Poisson's equation,

$$\begin{aligned}\nabla^2\phi &= e(\delta n_{e^-} - \delta n_{e^+}) - Ze\delta(\mathbf{r}) \\ &\approx \frac{4\alpha\phi(r)}{\pi}\int_0^\infty [N_-(E)+N_+(E)]\,\frac{\mathbf{p}^2}{E}\left(1+\frac{1}{v^2}\right)d|\mathbf{p}| - Ze\delta(\mathbf{r}),\end{aligned} \tag{7}$$

where $\alpha \equiv e^2/(4\pi)$ and $v = |\mathbf{p}|/E$. The approximate result in Eq. (7) is obtained by using Eq. (6) and performing integration by parts. The solution to Eq. (7) in the momentum space is

$$V(|\mathbf{k}|) = \int \phi(r)\exp(-i\mathbf{k}\cdot\mathbf{r})d^3\mathbf{r} = \frac{Ze}{\mathbf{k}^2\epsilon(|\mathbf{k}|)}, \tag{8}$$

where

$$\epsilon(|\mathbf{k}|) \approx 1 + \frac{4\alpha}{\pi\mathbf{k}^2}\int_0^\infty [N_-(E)+N_+(E)]\,\frac{\mathbf{p}^2}{E}\left(1+\frac{1}{v^2}\right)d|\mathbf{p}| \tag{9}$$

is the static dielectric function.

The electron screening effect also affects the propagation of photons in the $e^{\pm}$ plasma. For a photon of energy ω and momentum $\mathbf{k}$, the longitudinal component $\Pi_l(\omega, |\mathbf{k}|)$ of its polarization tensor to the first order in α [26] is

$$\Pi_l(\omega, |\mathbf{k}|) = \frac{4\alpha}{\pi} \int_0^\infty \left(\frac{\omega}{v|\mathbf{k}|} \ln \frac{\omega + v|\mathbf{k}|}{\omega - v|\mathbf{k}|} - 1 - \frac{\omega^2 - \mathbf{k}^2}{\omega^2 - v^2\mathbf{k}^2} \right) [N_-(E) + N_+(E)] \frac{\mathbf{p}^2}{E} d|\mathbf{p}|. \quad (10)$$

The static dielectric function $\epsilon(|\mathbf{k}|)$ is related to $\Pi_l(\omega, |\mathbf{k}|)$ for $\omega = 0$ as $\epsilon(|\mathbf{k}|) = 1 - \Pi_l(0, |\mathbf{k}|)/\mathbf{k}^2$, which gives the same result as Eq. (9) derived from the semiclassical approximation.

Note that Eq. (9) applies to all T and ρ/μ_e and is accurate to the first order in α [26]. The conditions in a massive star span a wide range of T and ρ/μ_e during its pre-supernova evolution. Figure 2 shows the evolutionary tracks of T and ρ/μ_e at the center for two stars of 15 and 25 $M_\odot$, respectively. The $(T, \rho/\mu_e)$ space can be approximately divided into four regions: (1) $T > 0.3m_e$ and $T > 0.3T_F$, where the $e^{\pm}$ gas is relativistic and non-degenerate or moderately degenerate (R, N/MD), (2) $0.3T_F < T < 0.3m_e$, where the gas is non-relativistic and non-degenerate or moderately degenerate (NR, N/MD), (3) $T < 0.3T_F$ and $T_F < m_e$, where the gas is non-relativistic and degenerate (NR, D), and (4) $T < 0.3T_F$ and $T_F > m_e$, where the gas is relativistic and degenerate (R, D). Here m_e is the electron mass and T_F is the electron Fermi temperature defined as

$$T_F \equiv \frac{\sqrt{p_F^2 + m_e^2} - m_e}{k_B} = 5.930 \times 10^9 \left\{ \left[1 + 1.018(\rho_6/\mu_e)^{2/3} \right]^{1/2} - 1 \right\} \text{ K}, \quad (11)$$

where $p_F = (3\pi^2 n_e)^{1/3}$ is the electron Fermi momentum, and ρ_6 is ρ in units of 10^6 g cm^{-3}. Figure 2 shows that massive stars undergoing core oxygen (O) burning encounter conditions at the boundary of the above four regions, for which Eq. (9) should be used to evaluate the static dielectric function $\epsilon(|\mathbf{k}|)$. We have checked that the approximate expressions adopted in Refs. [27, 28] give the same results as Eq. (9) only when positrons can be ignored [i.e., well within the (NR, ND), (NR, D), and (R,D) regions in Fig. 2]. We use Eq. (9) for $\epsilon(|\mathbf{k}|)$ in our calculations below.

B. Structure factor $S_\Gamma(|\mathbf{k}|)$

For the conditions of interest, $e^{\pm}$ can always be treated as in a gas state. They are scattered by the total (screened) Coulomb potential generated by all ions. When the tem-

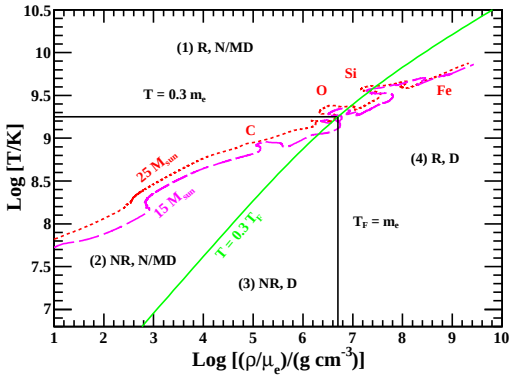

FIG. 2. Regions of the $(T, \rho/\mu_e)$ space where electrons are (1) relativistic and non-degenerate or moderately degenerate (R, N/MD), (2) non-relativistic and non-degenerate or moderately degenerate (NR, N/MD), (3) non-relativistic and degenerate (NR, D), and (4) relativistic and degenerate (R, D), respectively. Also shown are the evolutionary tracks of T and ρ/μ_e at the center for two stars of 15 and 25 $M_\odot$, respectively. The labels for the tracks indicate approximately stages of core C, O, and Si burning and Fe core formation, respectively.

perature is high and/or the matter density is low, the ions are also in the gas state and each ion can be treated independently. The total rate for electron-nucleus scattering is simply the sum over each single ion. However, the dense stellar interiors can give rise to condensed states with strong correlations among ions. Previous studies [27–30] showed that these ionic correlations have substantial effects on neutrino emission from electron-nucleus bremsstrahlung and, therefore, should be treated properly.

Correlation effects are described by the structure factor. Consider N ions located at $\mathbf{R}_i$ $(i = 1, 2, ..., N)$ in an OCP. The ionic number density is $n_I(\mathbf{r}) = \sum_i^N \delta(\mathbf{r} - \mathbf{R}_i)$. In the static case and by the Born approximation, the total electron-nucleus scattering amplitude is proportional to

$$V_{\rm tot}(\mathbf{k}) = V_{\rm eff}(|\mathbf{k}|) \int n_I(\mathbf{r}) \exp(-i\mathbf{k}\cdot\mathbf{r}) d^3\mathbf{r} = V_{\rm eff}(|\mathbf{k}|) \sum_i^N \exp(-i\mathbf{k}\cdot\mathbf{R}_i). \tag{12}$$

The total scattering rate is proportional to $|V_{\rm tot}(\mathbf{k})|^2 = |V_{\rm eff}(|\mathbf{k}|)|^2 \sum_{ij} \exp[-i\mathbf{k}\cdot(\mathbf{R}_i - \mathbf{R}_j)]$. Taking a time average of the OCP, we obtain

$$\left\langle |V_{\rm tot}(\mathbf{k})|^2 \right\rangle = |V_{\rm eff}(|\mathbf{k}|)|^2 \left\langle \sum_{ij} \exp[-i\mathbf{k}\cdot(\mathbf{R}_i - \mathbf{R}_j)] \right\rangle \equiv |V_{\rm eff}(|\mathbf{k}|)|^2 N S(\mathbf{k}), \tag{13}$$

where $S(\mathbf{k})$ is the static structure factor defined by the second equality. For an isotropic system, $S(\mathbf{k}) = S(|\mathbf{k}|)$. As a simple illustration, consider the gas state in which the correlations among ions are weak due to random thermal motion at high temperature and/or the feeble interaction between two distant ions at low density. For this case, $S(|\mathbf{k}|) \approx 1$ as only those terms with $i = j$ in the sum in Eq. (13) are not averaged out. Consequently, the total rate for electron-nucleus scattering in this case is just N times the rate for a single nucleus.

In general, the ionic state of an OCP can be characterized by the parameter

$$\Gamma \equiv \frac{Z^2 e^2}{a_I k_B T} = 0.2275 \frac{Z^2}{T_8} \left(\frac{\rho_6}{A}\right)^{1/3}, \tag{14}$$

where T_8 is T in units of 10^8 K, $a_I = [3/(4\pi \bar{n}_I)]^{1/3}$ is the ion-sphere radius, and $\bar{n}_I = \rho/(A m_u)$ is the mean ion number density. As can be seen from its definition, Γ measures the Coulomb interaction energy between two nearby ions relative to their thermal energy. The gas, liquid, and crystal lattice states correspond to $\Gamma \ll 1$, $1 \lesssim \Gamma \lesssim 180$, and $\Gamma > 180$, respectively. The structure factor is rather complex for the liquid and crystal lattice states. To indicate its dependence on Γ, we denote it as $S_\Gamma(|\mathbf{k}|)$.

Figure 3 shows contours of Γ for an OCP composed of ^{12}C or ^{56}Fe along with the evolutionary tracks of T and ρ/μ_e at the center for two stars of 15 and 25 $M_\odot$, respectively. It can be seen that ions are in the gas or liquid state ($\Gamma \lesssim 10$) during the pre-supernova evolution of massive stars. An analytic fit to the structure factor $S_\Gamma(|\mathbf{k}|)$ for an OCP was provided by Ref. [31] based on the results calculated from the modified hypernetted-chain equation for $0.1 \leq \Gamma \leq 225$ [32]. Although the fit was obtained for $1 \leq \Gamma \leq 225$, we find that its extension to $\Gamma < 1$ remains a good approximation to the results calculated in Ref. [32] even for $\Gamma = 0.1$. It also has the correct asymptotic behavior $S_\Gamma(|\mathbf{k}|) \to 1$ for $\Gamma \to 0$. Therefore, this fit is sufficient for our discussion on the spectra and rates for neutrino emission from electron-nucleus bremsstrahlung during the pre-supernova evolution of massive stars.

The crystal lattice state may be reached for $\Gamma \gtrsim 210$ during the cooling of dense stars [33]. The structure factor in this regime is needed for a general discussion of the conditions under which neutrino energy loss is dominated by electron-nucleus bremsstrahlung. Here new effects associated with the thermal motion of ions, the band structure of electrons [34], and multi-phonon processes [35] must be taken into account. We follow the discussion in Ref. [35] to calculate $S_\Gamma(|\mathbf{k}|)$ for the crystal lattice state and refer readers to that work for details. The resulting prescription gives similar values for $S_\Gamma(|\mathbf{k}|)$ to those from the fit in

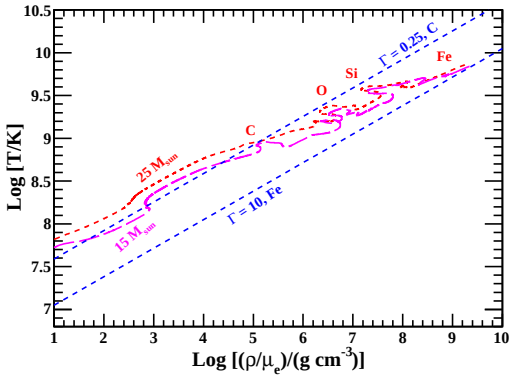

FIG. 3. Contours in the $(T, \rho/\mu_e)$ space corresponding to $\Gamma = 0.25$ for an OCP composed of ^{12}C and $\Gamma = 10$ for an OCP composed of ^{56}Fe. Also shown are the same two stellar evolutionary tracks as in Fig. 2.

Ref. [31] for $100 \lesssim \Gamma \lesssim 225$ [35]. In our calculations, we adopt the fit in Ref. [31] for $\Gamma \leq 180$ and the prescription in Ref. [35] for $\Gamma > 180$.

C. Matrix elements and energy-differential rates

We now calculate the matrix elements for ν_e and $\bar{\nu}_e$ emission from electron-nucleus bremsstrahlung. We first ignore ionic correlations. The amplitude for the Z^0-exchange diagrams can be written in standard notation of the electroweak theory as

$$i\mathcal{M}_{Z^0} = -\frac{iZe^2G_F^2}{2\sqrt{2}}\frac{f(|\mathbf{k}|)}{\mathbf{k}^2\epsilon(|\mathbf{k}|)}\left[\bar{u}_e(p')\gamma^\alpha(a+b\gamma^5)(\not{p}+\not{k}-m_e)^{-1}\gamma^0 u_e(p)\bar{u}_\nu(q)\gamma_\alpha(1-\gamma^5)v_{\bar{\nu}}(q')\right.$$
$$\left.+\bar{u}_e(p')\gamma^0(\not{p}'-\not{k}-m_e)^{-1}\gamma^\alpha(a+b\gamma^5)u_e(p)\bar{u}_\nu(q)\gamma_\alpha(1-\gamma^5)v_{\bar{\nu}}(q')\right], \quad (15)$$

where G_F is the Fermi coupling constant, $a = -1 + 4s_W^2$, $s_W \equiv \sin\theta_W$ with θ_W being the Weinberg angle, $b = 1$, γ^α $(\alpha = 0, 1, 2, 3)$ and γ^5 refer to the Dirac gamma matrices, u and v are spinors, and the four-momenta k, p, p', q, and q' are as labeled in Fig. 1. Note that the four-momentum for the virtual photon is $k = (0, \mathbf{k})$.

The amplitude for the W-exchange diagrams can be arranged to have a similar structure to that for the Z^0-exchange diagrams via Fierz transformations. The total amplitude for

both types of diagrams is

$$
\begin{aligned}
i\mathcal{M} =& i(\mathcal{M}_{Z^0}+\mathcal{M}_W) \\
=& -\frac{iZe^2G_F}{\sqrt{2}}\frac{f(|\mathbf{k}|)}{\mathbf{k}^2\epsilon(|\mathbf{k}|)}\left[\bar{u}_e(p')\gamma^\alpha(C_V-C_A\gamma^5)(\not{p}+\not{k}-m_e)^{-1}\gamma_0 u_e(p)\bar{u}_\nu(q)\gamma_\alpha(1-\gamma^5)v_{\bar{\nu}}(q')\right. \\
&\left.+\,\bar{u}_e(p')\gamma_0(\not{p}'-\not{k}-m_e)^{-1}\gamma^\alpha(C_V-C_A\gamma^5)u_e(p)\bar{u}_\nu(q)\gamma_\alpha(1-\gamma^5)v_{\bar{\nu}}(q')\right], \qquad (16)
\end{aligned}
$$

where $C_V=(1+4s_W^2)/2$ and $C_A=1/2$. After averaging over the fermion spins in the initial state and summing over those in the final state, we obtain the effective squared matrix element

$$
\begin{aligned}
|\mathcal{M}|^2_{\rm eff} =& \frac{Z^2e^4G_F^2}{4}\frac{[f(|\mathbf{k}|)]^2}{[\mathbf{k}^2\epsilon(|\mathbf{k}|)]^2} \\
&\times \mathrm{Tr}\left\{(\not{p}'+m_e)\left[\gamma^\alpha(C_V-C_A\gamma^5)\frac{\not{Q}_1+m_e}{\beta_1}\not{\epsilon}_B+\not{\epsilon}_B\frac{\not{Q}_2+m_e}{\beta_2}\gamma^\alpha(C_V-C_A\gamma^5)\right](\not{p}+m_e)\right. \\
&\left.\times\left[(C_V+C_A\gamma^5)\gamma^\beta\frac{\not{Q}_2+m_e}{\beta_2}\not{\epsilon}_B+\not{\epsilon}_B\frac{\not{Q}_1+m_e}{\beta_1}(C_V+C_A\gamma^5)\gamma^\beta\right]\right\} \\
&\times \mathrm{Tr}\left[\not{q}\gamma_\alpha(1-\gamma^5)\not{q}'(1+\gamma^5)\gamma_\beta\right], \qquad (17)
\end{aligned}
$$

where $Q_1\equiv p+k$, $Q_2\equiv p'-k$, $\beta_1\equiv 2k\cdot p-\mathbf{k}^2$, and $\beta_2\equiv -2k\cdot p'-\mathbf{k}^2$. Note that we have defined an artificial polarization four-vector $\epsilon_B=(1,0,0,0)$ to make the result similar to that for photo-neutrino emission [2, 21]. With the definition of I_i^B $(i=1,2,3)$ in Appendix A, Eq. (17) can be rewritten as

$$
|\mathcal{M}|^2_{\rm eff}=4Z^2e^4G_F^2\frac{[f(|\mathbf{k}|)]^2}{[\mathbf{k}^2\epsilon(|\mathbf{k}|)]^2}\left[(C_V^2+C_A^2)I_1^B+(C_V^2-C_A^2)I_2^B+C_VC_AI_3^B\right]. \qquad (18)
$$

1. *OCP*

Including the structure factor $S_\Gamma(|\mathbf{k}|)$ to account for ionic correlations and integrating over the phase space of the initial and final states, we obtain the energy-differential rate per unit volume for ν_e emission from electron-nucleus bremsstrahlung in an OCP as

$$
\begin{aligned}
F_{\nu_e}(E_\nu) =& \frac{\rho}{Am_u}\int\frac{2d^3\mathbf{p}}{2E(2\pi)^3}N_-(E)\int\frac{d^3\mathbf{k}}{(2\pi)^3}S_\Gamma(|\mathbf{k}|)\int\frac{d^3\mathbf{p}'}{2E'(2\pi)^3}\left[1-N_-(E')\right] \\
&\times\int\frac{d^3\mathbf{q}'}{2E'_\nu(2\pi)^3}\int\frac{E_\nu^2d\Omega_{\mathbf{q}}}{2E_\nu(2\pi)^3}(2\pi)^4\delta(p+k-p'-q-q')|\mathcal{M}|^2_{\rm eff} \\
=& \frac{\rho}{Am_u}\int\frac{2d^3\mathbf{p}}{2E(2\pi)^3}N_-(E)\int\frac{d^3\mathbf{k}}{(2\pi)^3}S_\Gamma(|\mathbf{k}|)\int\frac{d^3\mathbf{p}'}{2E'(2\pi)^3}\left[1-N_-(E')\right]\frac{\int d\varphi|\mathcal{M}|^2_{\rm eff}}{16\pi^2|\mathbf{P}|}, \qquad (19)
\end{aligned}
$$

where $\mathbf{P} \equiv \mathbf{p} + \mathbf{k} - \mathbf{p}'$, and $\Omega_{\mathbf{q}}$ is the solid angle for the ν_e momentum $\mathbf{q}$ with φ being the azimuth angle around $\mathbf{P}$. Note that the δ function in the above equation is disposed of by integration over the $\bar{\nu}_e$ momentum $\mathbf{q}'$ and the polar angle of $\mathbf{q}$ with respect to $\mathbf{P}$. For ν_x, only Z^0-exchange diagrams contribute, and the corresponding differential rate $F_{\nu_x}(E_\nu)$ is obtained by replacing C_V and C_A in $|\mathcal{M}|^2_{\rm eff}$ [see Eq. (18)] with a and $-b$ as defined for Eq. (15), respectively.

Note that only the neutrino four-momentum q shows up explicitly in the expressions for I_i^B $(i = 1, 2, 3)$ [see Eqs. (A1)–(A4)] as the antineutrino four-momentum q' has been evaluated by applying conservation of energy and momentum. If q' is kept instead of q, the new expressions have the same form but with q' replacing q and an opposite sign for I_3^B. In other words, I_1^B and I_2^B are symmetric while I_3^B is antisymmetric under the exchange of q and q'. Therefore, a simple way to obtain $F_{\bar{\nu}_\alpha}(E_\nu)$ is to change the sign of the contribution from the I_3^B term in $F_{\nu_\alpha}(E_\nu)$. This sign change makes the neutrino and antineutrino spectra somewhat different. However, when integrated over the ν_α and $\bar{\nu}_\alpha$ phase space to obtain the total rates of emission R_{ν_α} $(R_{\bar{\nu}_\alpha})$ and energy loss Q_{ν_α} $(Q_{\bar{\nu}_\alpha})$ in ν_α $(\bar{\nu}_\alpha)$, the I_3^B term does not contribute. The contributions from the I_1^B and I_2^B terms always ensure that $R_{\nu_\alpha} = R_{\bar{\nu}_\alpha}$ and $Q_{\nu_\alpha} = Q_{\bar{\nu}_\alpha}$.

Finally, positrons can also scatter on nuclei to produce $\nu_\alpha\bar{\nu}_\alpha$ pairs. For the same incoming and outgoing four-momenta p and p', respectively, the amplitudes of positron-nucleus bremsstrahlung can be obtained by interchanging p and $-p'$ in the results for electron-nucleus bremsstrahlung. The terms I_1^B and I_2^B are symmetric while I_3^B is antisymmetric under this interchange. Therefore, the differential rates for positron-nucleus bremsstrahlung can be obtained by replacing $N_-(E)$ $[N_-(E')]$ with $N_+(E)$ $[N_+(E')]$ and changing the sign of I_3^B in Eq. (19). We include the contributions from both electrons and positrons to bremsstrahlung neutrino emission in our numerical results.

2. Multi-Component Plasma

Stellar matter typically consists of more than one nuclear species, and thus corresponds to a multi-component plasma (MCP). To extend our results to this case, we follow Ref. [36] and treat the different nuclear components independently. The state of nuclei (Z_j, A_j) is

determined by

$$\Gamma_j = \frac{Z_j^2 e^2}{a_j k_B T} = 0.2275 \frac{Z_j^{5/3}}{T_8} \left(\rho_6 \sum_i \frac{x_i Z_i}{A_i} \right)^{1/3}, \tag{20}$$

where a_j is defined by

$$\frac{4\pi}{3} a_j^3 \sum_i \frac{x_i \rho}{A_i m_u} Z_i = Z_j, \tag{21}$$

and x_i is the mass fraction of nuclei (Z_i, A_i). For an OCP, Γ_j and a_j reduce to Γ [see Eq. (14)] and a_I, respectively. For the jth component, the same structure factor $S_{\Gamma_j}(|\mathbf{k}|)$ as for an OCP is used to account for ionic correlations. Summing the contributions from each component incoherently, we can generalize the energy-differential rate in Eq. (19) as

$$F_{\nu_e}(E_\nu) = \sum_j \frac{x_j \rho}{A_j m_u} \int \frac{2 d^3\mathbf{p}}{2E(2\pi)^3} N_-(E) \int \frac{d^3\mathbf{k}}{(2\pi)^3} S_{\Gamma_j}(|\mathbf{k}|) \int \frac{d^3\mathbf{p}'}{2E'(2\pi)^3} \left[1 - N_-(E')\right] \frac{\int d\varphi |\mathcal{M}_j|^2_{\rm eff}}{16\pi^2 |\mathbf{P}|}, \tag{22}$$

where $|\mathcal{M}_j|^2_{\rm eff}$ is given by Eq. (18) with Z replaced by Z_j.

The above approximate method of treating an MCP has some limitation [37]. However, for the neutrino energy range of interest, $E_\nu \gtrsim 0.1$ MeV, the results based on this method are consistent with those from simulations based on molecular dynamics [38]. The same method has also been adopted to treat neutrino-nucleus scattering during stellar core collapse [39].

III. COMPARISON OF SPECTRA AND RATES FOR THERMAL NEUTRINO EMISSION PROCESSES

The energy-differential rate in Eq. (19) is highly non-trivial to calculate. Our numerical computation proceeds as follows. We pick $\mathbf{p}$ as the z-direction and define a coordinate system. By specifying $|\mathbf{p}|$, $\mathbf{k}$, and $\mathbf{p}'$, we fix $\mathbf{P} = \mathbf{p} + \mathbf{k} - \mathbf{p}'$ and the polar angle of $\mathbf{q}$ with respect to $\mathbf{P}$ (through energy and momentum conservation). By further specifying the azimuthal angle φ of $\mathbf{q}$ around $\mathbf{P}$, all the vectors involved in the effective squared matrix element $|\mathcal{M}|^2_{\rm eff}$ are fixed. Therefore, the energy-differential rate is an eight-dimensional integral over φ, $\mathbf{p}'$, $\mathbf{k}$, and $|\mathbf{p}|$. We use the Vegas Monte Carlo algorithm encoded in the CUBA library [40] to evaluate all the multidimensional integrals in this work.

A. Effects of ionic correlations on bremsstrahlung neutrino emission

As discussed in Sec. II B, ionic correlations complicate the calculation of the energy-differential rate for bremsstrahlung neutrino emission. Taking $T = 4 \times 10^9$ K and $\rho/\mu_e = 10^8$ g cm^{-3}, we show in Fig. 4 the ratio of the rate $F_{\bar{\nu}_e}$ with ionic correlations to the rate $F^0_{\bar{\nu}_e}$ without such correlations as a function of $\bar{\nu}_e$ energy E_ν for an OCP composed of ^{28}Si or ^{56}Fe with $\Gamma \approx 2.2$ or 6, respectively. It can be seen that ionic correlations reduce the energy-differential rate by a factor of ~ 2 at low energies and by a factor of ~ 1.3 at high energies. This result is not sensitive to the composition of the OCP and we have checked that it holds true generally for $\Gamma \lesssim 10$, which is relevant for massive stars during their pre-supernova evolution (see Fig. 3). At $E_\nu \geq 1.8$ MeV, for which $\bar{\nu}_e$ can be detected through capture on protons, $F_{\bar{\nu}_e}/F^0_{\bar{\nu}_e}$ varies very slowly and is close to 0.7.

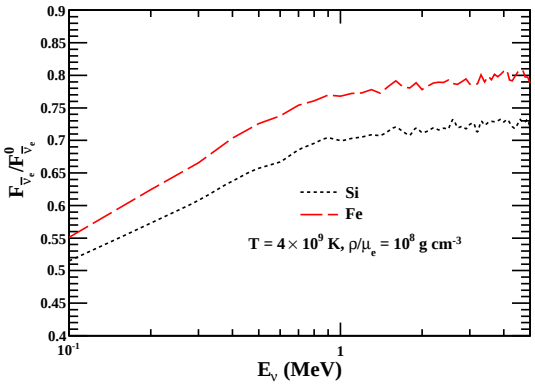

FIG. 4. Effects of ionic correlations on bremsstrahlung neutrino emission. The ratio of the rate $F_{\bar{\nu}_e}$ with ionic correlations to the rate $F^0_{\bar{\nu}_e}$ without such correlations is shown as a function of $\bar{\nu}_e$ energy E_ν for an OCP composed of ^{28}Si or ^{56}Fe, respectively.

B. Energy-differential rates

As mentioned in the Introduction, energy-differential rates for $e^\pm$ pair annihilation, plasmon decay, and photo-neutrino emission have been studied in detail by previous works [13, 16, 20–24]. We are not aware of a detailed discussion of the energy-differential rate for bremsstrahlung neutrino emission in the literature. We now discuss this in comparison with the other thermal emission processes listed above. We follow the standard procedures to

calculate the energy-differential rates for $e^{\pm}$ annihilation [16], plasmon decay [20, 23], and photo-neutrino emission [21]. Although details are not presented here, we have used different expressions for the squared amplitudes from those in the literature by enforcing energy and momentum conservation in different ways and we have adopted different integration procedures. Therefore, our results for these three processes provide an independent check on the previous results.

For specific numerical examples, we consider four sets of temperature and density $(T_9, \rho_7/\mu_e) = (0.87, 8.5 \times 10^{-3})$, $(2.3, 0.36)$, $(3.9, 1.9)$, $(7.1, 2.5 \times 10^2)$, which are representative of massive stellar cores during C burning, at O depletion, at silicon (Si) depletion, and immediately prior to collapse, respectively [41]. Here T_9 is T in units of 10^9 K and ρ_7 is ρ in units of 10^7 g cm^{-3}. For calculating the rates for bremsstrahlung neutrino emission, we simply assume an OCP composed of ^{16}O, ^{28}Si, ^{56}Fe, and ^{56}Fe, respectively, which approximately corresponds to the composition for the selected stages of stellar evolution. Contributions from other coexisting nuclei can be included in a straightforward manner as shown in Eq. (22). Because Γ_j does not vary much over the typical composition, S_{Γ_j} has similar effects on neutrino emission for different components, and the contribution from each component is approximately proportional to $x_j Z_j^2/A_j$. As the total mass fraction of the subdominant nuclei is typically $\lesssim 20\%$, we find that a simple OCP treatment based on the dominant species introduces errors only at the level of $\sim 10\%$. The energy-differential rates $F_{\bar{\nu}_e}$ in units of cm^{-3} MeV^{-1} s^{-1} for $\bar{\nu}_e$ emission from the above four processes are shown as functions of $\bar{\nu}_e$ energy E_ν in Fig. 5. It can be seen that the differential rate for $e^{\pm}$ pair annihilation always dominates at high energies, while at low energies, the rates for the other processes become comparable or take over. Similar to plasmon decay and photo-neutrino emission, bremsstrahlung mostly produces sub-MeV neutrinos during the pre-supernova evolution of massive stars. It is interesting to note that bremsstrahlung and plasmon decay have similar spectral shapes, most likely due to similar phase spaces for the outgoing particles. The comparison of F_{ν_e} for the thermal emission processes is very similar to that of $F_{\bar{\nu}_e}$ and, therefore, is not shown here.

Partly because of the conversion of $e^{\pm}$ rest mass into neutrino energy, pair annihilation always produces the highest average neutrino energy. For example, the average $\bar{\nu}_e$ energy from pair annihilation in a non-degenerate and non-relativistic gas of $e^{\pm}$ can be estimated as $\langle E_{\bar{\nu}_e} \rangle \sim m_e + 3k_B T$. In general, the average neutrino energies for different thermal emission

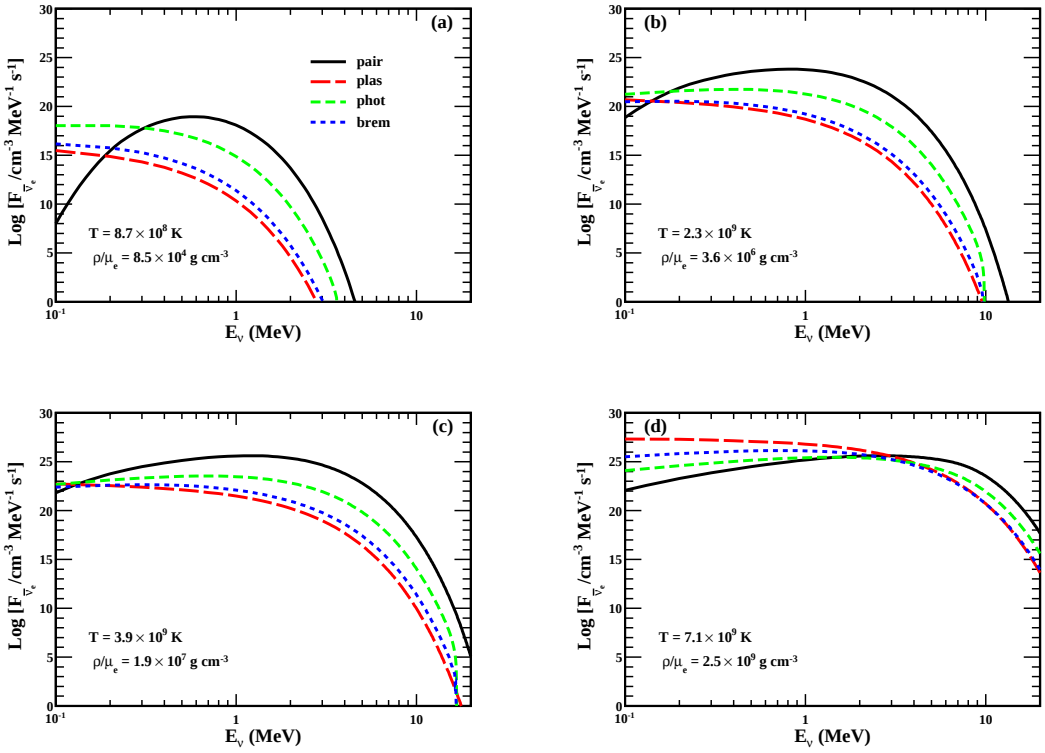

FIG. 5. Comparison of energy-differential rates $F_{\bar{\nu}_e}$ as functions of $\bar{\nu}_e$ energy E_ν for $e^\pm$ pair annihilation ("pair"), plasmon decay ("plas"), photo-neutrino emission ("phot"), and bremsstrahlung neutrino emission ("brem"). The conditions indicated are representative of massive stellar cores (a) during C burning, (b) at O depletion, (c) at Si depletion, and (d) immediately prior to collapse.

processes are nontrivial functions of both temperature and density. Table I gives the average $\bar{\nu}_\alpha$ energies $\langle E_{\bar{\nu}_\alpha}\rangle$ for these processes along with the corresponding net emission rates $R_{\bar{\nu}_\alpha}$ in units of cm^{-3} s^{-1} at the four selected stages of stellar evolution. It can be seen that both $R_{\bar{\nu}_\alpha}$ and $\langle E_{\bar{\nu}_\alpha}\rangle$ generally increase for all the processes as the star evolves. However, the net emission rates for pair annihilation are severely suppressed immediately prior to core collapse because of strong electron degeneracy. This allows other processes to compete for energy loss. Table I shows that $\langle E_{\bar{\nu}_e}\rangle = \langle E_{\bar{\nu}_x}\rangle$ for plasmon decay, but in general $\langle E_{\bar{\nu}_e}\rangle$ is slightly lower than $\langle E_{\bar{\nu}_x}\rangle$ for the other processes. We note that $\langle E_{\nu_\alpha}\rangle = \langle E_{\bar{\nu}_\alpha}\rangle$ for all thermal emission processes.

We now consider the potential detection of neutrinos from massive stars during their pre-supernova evolution. As an example, we focus on the detection of $\bar{\nu}_e$ through capture

TABLE I. Comparison of rates and characteristic energies for thermal neutrino emission processes. Four sets of conditions representative of massive stellar cores during C burning, at O depletion, at Si depletion, and immediately prior to collapse are chosen. For each case, results for $e^{\pm}$ pair annihilation, plasmon decay, photo-neutrino emission, and bremsstrahlung neutrino emission are given in four consecutive rows. $R_{\bar{\nu}_{e,x}}$ and $\langle E_{\bar{\nu}_{e,x}} \rangle$ are the net emission rates and average energies of $\bar{\nu}_{e,x}$, respectively. $R^{>}_{\bar{\nu}_{e,x}}$ and $\bar{E}^{>}_{\bar{\nu}_{e,x}}$ are the net rates and average energies for those $\bar{\nu}_{e,x}$ with energy above $E_{\rm th} \approx 1.8$ MeV. $\bar{E}^{\rm det}_{\bar{\nu}_{e,x}}$ is an effective energy for $\bar{\nu}_e$ detection, as defined in Eq. (23). $R^{>}_{\bar{\nu}_{e,x}}$ are in units of cm^{-3} s^{-1}, and the characteristic energies $\langle E_{\bar{\nu}_{e,x}} \rangle$, $\bar{E}^{>}_{\bar{\nu}_{e,x}}$, and $\bar{E}^{\rm det}_{\bar{\nu}_{e,x}}$ are in units of MeV.

$(T_9, \rho_7/\mu_e)$	$\log(R_{\bar{\nu}_{e,x}})$	$\langle E_{\bar{\nu}_{e,x}} \rangle$	$\log(R^{>}_{\bar{\nu}_{e,x}})$	$\bar{E}^{>}_{\bar{\nu}_{e,x}}$	$\bar{E}^{\rm det}_{\bar{\nu}_{e,x}}$
$(0.87, 8.5 \times 10^{-3})$	18.57, 17.22	0.648, 0.684	13.60, 12.58	1.892, 1.893	1.886, 1.888
	15.05, 12.24	0.061, 0.061	4.59, 1.79	1.877, 1.877	1.872, 1.872
	17.54, 17.15	0.227, 0.226	9.69, 9.29	1.885, 1.895	1.879, 1.879
	15.44, 14.96	0.131, 0.136	5.78, 5.58	1.886, 1.898	1.876, 1.877
$(2.3, 0.36)$	23.79, 22.86	1.006, 1.089	22.45, 21.66	2.088, 2.092	2.118, 2.127
	20.21, 17.40	0.176, 0.176	16.27, 13.46	1.993, 1.993	2.019, 2.019
	21.64, 21.13	0.607, 0.620	19.49, 19.01	2.036, 2.032	2.072, 2.073
	20.20, 19.69	0.348, 0.376	16.92, 16.67	2.025, 2.017	2.036, 2.046
$(3.9, 1.9)$	25.82, 25.04	1.524, 1.630	25.30, 24.58	2.372, 2.399	2.488, 2.510
	22.35, 19.54	0.314, 0.314	20.03, 17.22	2.139, 2.139	2.199, 2.199
	23.66, 23.08	1.040, 1.089	22.70, 22.18	2.281, 2.295	2.363, 2.373
	22.54, 21.97	0.592, 0.661	20.77, 20.43	2.187, 2.201	2.234, 2.279
$(7.1, 2.5 \times 10^2)$	26.24, 25.55	3.558, 4.150	26.17, 25.50	3.953, 4.472	4.387, 4.922
	27.23, 24.42	0.765, 0.765	26.16, 23.35	2.457, 2.457	2.620, 2.620
	25.91, 25.25	2.177, 2.404	25.65, 25.03	3.064, 3.231	3.379, 3.603
	26.39, 25.73	1.322, 1.413	25.77, 25.17	2.610, 2.632	2.758, 2.848

on protons, $\bar{\nu}_e + p \to n + e^+$, which has a threshold of $E_{\rm th} \approx 1.8$ MeV. The net emission rate $R^{>}_{\bar{\nu}_\alpha}$ and average energy $\bar{E}^{>}_{\bar{\nu}_\alpha}$ for $\bar{\nu}_\alpha$ with energy above $E_{\rm th}$ are given in Table I for each thermal emission process at the four selected stages of stellar evolution. For consideration of detection, we define an effective energy $\bar{E}^{\rm det}_{\bar{\nu}_\alpha}$ through

$$\sigma_{\bar{\nu}_e p}(\bar{E}^{\rm det}_{\bar{\nu}_\alpha}) \equiv \frac{\int^{\infty}_{E_{\rm th}} \sigma_{\bar{\nu}_e p}(E_\nu) F_{\bar{\nu}_\alpha}(E_\nu) dE_\nu}{\int^{\infty}_{E_{\rm th}} F_{\bar{\nu}_\alpha}(E_\nu) dE_\nu} = \frac{1}{R^{>}_{\bar{\nu}_\alpha}} \int^{\infty}_{E_{\rm th}} \sigma_{\bar{\nu}_e p}(E_\nu) F_{\bar{\nu}_\alpha}(E_\nu) dE_\nu, \tag{23}$$

where $\sigma_{\bar{\nu}_e p}(E_\nu) \propto (E_\nu - \Delta)\sqrt{(E_\nu - \Delta)^2 - m_e^2}$, with $\Delta = 1.293$ MeV being the neutron-proton mass difference, is the cross section for capture of $\bar{\nu}_e$ with energy E_ν. Note that $\bar{E}^{\rm det}_{\bar{\nu}_\alpha}$ is also introduced for $\bar{\nu}_x$ in consideration of flavor oscillations between $\bar{\nu}_x$ and $\bar{\nu}_e$. If flavor oscillations are independent of energy, then the net emission rate $R^{>}_{\bar{\nu}_\alpha}$ above the detection threshold contributes to the $\bar{\nu}_e + p \to n + e^+$ event rate in proportion to the product of $R^{>}_{\bar{\nu}_\alpha}$ and the detection cross section at a single energy $\bar{E}^{\rm det}_{\bar{\nu}_\alpha}$. This provides an efficient way to estimate the event rate without referring to the detailed emission spectra. The value of $\bar{E}^{\rm det}_{\bar{\nu}_\alpha}$ for each thermal emission process is also given in Table I. It can be seen that $\bar{E}^{\rm det}_{\bar{\nu}_\alpha}$ for all thermal emission processes increase somewhat as the star ages and that $\bar{E}^{\rm det}_{\bar{\nu}_\alpha}$ for pair annihilation and photo-neutrino emission increase significantly immediately prior to core collapse. These increases favor the detection of $\bar{\nu}_e$ from later stages of stellar evolution because $\sigma_{\bar{\nu}_e p}(\bar{E}^{\rm det}_{\bar{\nu}_\alpha})$ increases sharply for $\bar{E}^{\rm det}_{\bar{\nu}_\alpha}$ close to $E_{\rm th}$. Note that $\bar{E}^{\rm det}_{\bar{\nu}_e} \approx \bar{E}^{\rm det}_{\bar{\nu}_x}$ except for the case of pair annihilation immediately prior to core collapse.

We have given the relevant information for both $\bar{\nu}_e$ and $\bar{\nu}_x$ in Table I in order to estimate the effect of $\bar{\nu}_e \rightleftharpoons \bar{\nu}_x$ flavor transformation caused by the MSW mechanism in massive stars. When flavor evolution is adiabatic, the survival probability p of $\bar{\nu}_e$ is insensitive to neutrino energy and can be estimated as $p_{\rm NH} = \cos^2\theta_{12}\cos^2\theta_{13} \approx 0.7$ for the normal mass hierarchy (NH) and $p_{\rm IH} = \sin^2\theta_{13} \approx 0.025$ for the inverted mass hierarchy (IH) [42], where θ_{12} and θ_{13} are the vacuum mixing angles. The $\bar{\nu}_e$ event rate is proportional to $pR^{>}_{\bar{\nu}_e}\sigma(\bar{E}^{\rm det}_{\bar{\nu}_e}) + (1-p)R^{>}_{\bar{\nu}_x}\sigma(\bar{E}^{\rm det}_{\bar{\nu}_x})$. Table I shows that $R^{>}_{\bar{\nu}_\alpha}$ is comparable for all thermal emission processes only for the stage immediately prior to core collapse, and $R^{>}_{\bar{\nu}_\alpha}$ for pair annihilation is always the largest for all the previous stages. Taking into account that pair annihilation also has the highest $\bar{E}^{\rm det}_{\bar{\nu}_\alpha}$ (see Table I), we conclude that it is the dominant source for the $\bar{\nu}_e$ signal from the thermal emission processes.

IV. COMPARISON OF ENERGY LOSS RATES FOR THERMAL NEUTRINO EMISSION PROCESSES

It is straightforward to calculate the total neutrino energy loss rate per unit volume

$$Q = \sum_{\alpha=e,\mu,\tau} \int E_\nu [F_{\nu_\alpha}(E_\nu) + F_{\bar{\nu}_\alpha}(E_\nu)] dE_\nu \tag{24}$$

for bremsstrahlung and other thermal emission processes. For simplicity, we assume an OCP composed of ^{56}Fe for calculating the rates for bremsstrahlung neutrino emission in this section. As the effects of ionic correlations are not very sensitive to composition (see Fig. 4), results for a different composition can be approximately obtained from those for ^{56}Fe through scaling with Z^2/A [see Eq. (19)]. In Fig. 6, we compare our calculated total energy loss rates for individual processes with the fitting formulas [10] widely used in stellar evolution models. We show Q as a function of ρ/μ_e (between 10 and 10^{11} g cm^{-3}) for $T = 10^8$, 10^9, 10^{10}, and 10^{11} K, respectively. It can be seen that our results for bremsstrahlung neutrino emission are in good agreement with the fitting formulas, which provides an indirect check on the soundness of our energy-differential rates. The small differences come from the following several factors. We have used a more recent and slightly different structure factor $S_\Gamma(|\mathbf{k}|)$ and a more general static dielectric function $\epsilon(|\mathbf{k}|)$. We have also included the contributions from positron-nucleus bremsstrahlung. In addition, the fitting formulas of Ref. [10] have intrinsic uncertainties in reproducing the underlying numerical results.

In consideration of the total neutrino energy loss rates for pair annihilation, plasmon decay, and photo-neutrino emission, we note that by design, the fitting formulas for a process are generally only accurate in the region where this process dominates. This accounts for the large discrepancies between our results and the fitting formulas in the regions where the latter fail, especially for plasmon decay and photo-neutrino emission. However, when summed over all thermal emission processes, our results are consistent with the fitting formulas within 5%–10%. Our results are in good agreement with the more up-to-date studies [13, 20–23]. These and our calculations have used improved treatment of plasmon dispersion relations and electrostatic screening for the relevant processes. The corresponding results are more accurate and should be used instead of the fitting formulas when individual thermal emission processes are of concern.

We define the domain of dominance for a process as the region in the $(T, \rho/\mu_e)$ space where

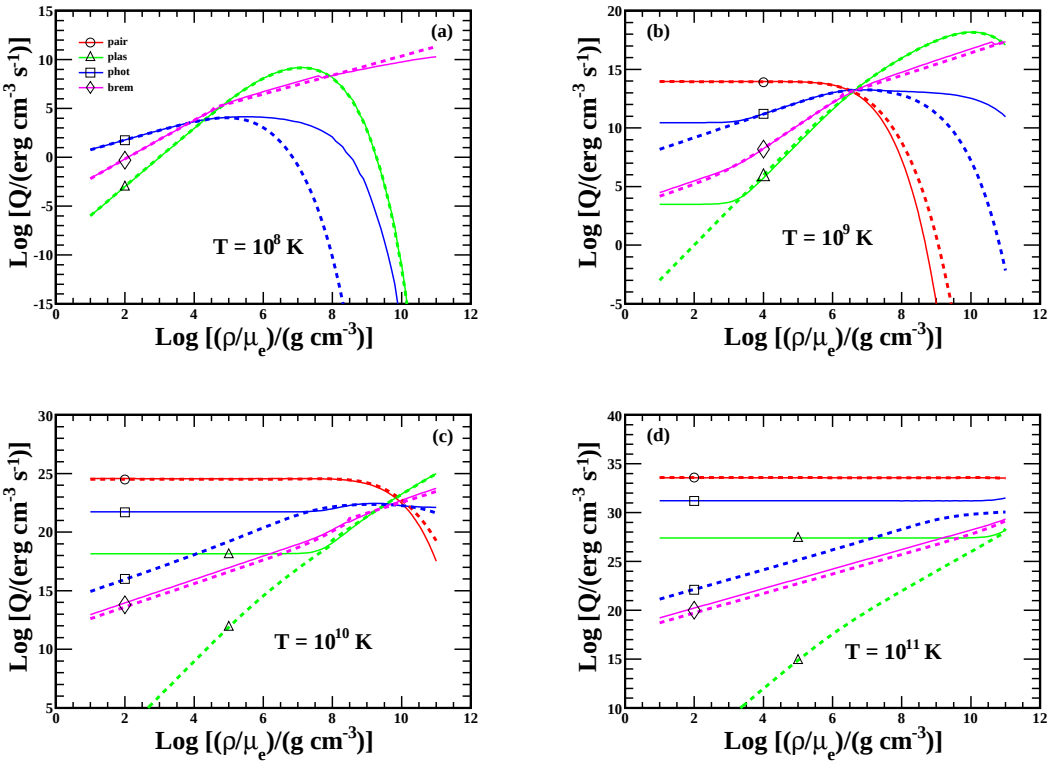

FIG. 6. Comparison of energy loss rates Q as functions of ρ/μ_e at (a) $T = 10^8$, (b) 10^9, (c) 10^{10}, and (d) 10^{11} K for $e^{\pm}$ pair annihilation ("pair", ◯), plasmon decay ("plas", △), photo-neutrino emission ("phot", □), and bremsstrahlung neutrino emission ("brem", ♢). Solid curves are our calculated results while dashed curves are from the fitting formulas of Ref. [10]. Note that $e^{\pm}$ pair annihilation is highly suppressed at $T = 10^8$ K and the corresponding energy loss rate is not shown in (a).

this process contributes at least 90% of the total neutrino energy loss rate summed over all the thermal emission processes. These domains are shown in Fig. 7 based on our results except for the recombination process, for which the fitting formulas [10] are used. The energy loss rate for pair annihilation is very sensitive to temperature and density. It dominates when the temperature is sufficiently high for producing $e^{\pm}$ pairs and the density is sufficiently low that positrons are not suppressed by degeneracy. When electrons are strongly degenerate, plasmon decay, photo-neutrino emission, and especially pair annihilation are suppressed. In this case, bremsstrahlung neutrino emission becomes dominant. When this occurs, ionic correlations are important and can reduce the energy loss rate by a factor of $\sim$ 2–10. We

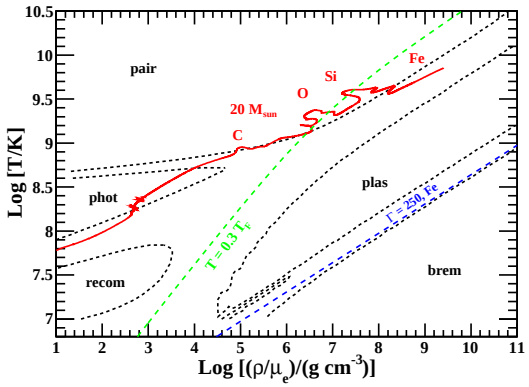

FIG. 7. Domain of dominance where a thermal neutrino emission process contributes at least 90% of the total energy loss rate. Our calculated rates are used for $e^{\pm}$ pair annihilation ("pair"), plasmon decay ("plas"), photo-neutrino emission ("phot"), and bremsstrahlung neutrino emission ("brem") while the fitting formulas of Ref. [10] are used for the recombination process ("recom"). An OCP composed of ^{56}Fe is assumed for calculating the rate for bremsstrahlung neutrino emission. Similar to Figs. 2 and 3, also shown are the evolutionary track of the central temperature and density for a $20\,M_{\odot}$ star, the curve for $T = 0.3T_F$, and the contour for $\Gamma = 250$ for an OCP composed of ^{56}Fe.

note that plasmon decay dominates in two regions. The transverse decay modes play a key role in the larger region while the longitudinal decay mode takes over in the much smaller region.

V. DISCUSSION AND CONCLUSIONS

We have presented a detailed derivation of the energy-differential rate for neutrino emission from electron-nucleus bremsstrahlung (Sec. II), taking into account the effects of electron screening and ionic correlations. We have compared the energy-differential and the net rates, as well as the average $\bar{\nu}_e$ and $\bar{\nu}_x$ energies, for this and other thermal neutrino emission processes over a wide range of temperature and density (Sec. III). We have also compared our updated energy loss rates for individual thermal neutrino emission processes with the fitting formulas of Ref. [10] and determined the temperature and density domain in which each process dominates (Sec. IV). We find that similar to plasmon decay and photo-neutrino emission, bremsstrahlung mostly produces sub-MeV neutrinos during the pre-supernova evo-

lution of massive stars. Our results on the neutrino energy loss rates are in good agreement with previous studies.

As discussed by previous studies [12–17], neutrino emission during the pre-supernova evolution of massive stars can provide a potential test of stellar models or at least give advance warning for core-collapse supernovae. While neutrino emission from $\beta^{\pm}$ decay and $e^{\pm}$ capture [24, 43] should be taken into account for a full study, we expect that $\bar{\nu}_e$ signals from the thermal processes discussed here always dominate except for the last hour or so prior to a supernova explosion. Figure 7 and Table I serve as approximate guides to the relative importance of each thermal neutrino emission process during the pre-supernova evolution of massive stars. With the largest $\bar{E}_{\bar{\nu}}^{\rm det}$ and $R_{\bar{\nu}}^{>}$, pair annihilation is always the dominant source of pre-supernova $\bar{\nu}_e$ signals for massive stars during core C burning and afterwards. For bremsstrahlung neutrino emission, we note that its domain of dominance is far from the evolutionary track of the central temperature and density for a $20\,M_{\odot}$ star, and therefore expect that it contributes only a small fraction of the $\bar{\nu}_e$ events. However, this domain overlaps with the conditions encountered during the cooling of neutron stars produced by the core collapse of massive stars. We refer readers to Refs. [35, 44] for more detailed discussions of bremsstrahlung neutrino emission relevant for neutron star cooling.

In general, significant thermal neutrino emission occurs throughout the hot and dense interior of a massive star during core C burning and afterwards. A proper estimate of the $\bar{\nu}_e$ signal from the pre-supernova evolution of the star requires a model that gives the radial profiles of temperature, density, and composition as well as the corresponding time evolution. We refer readers to Ref. [13] for a detailed study on the $\bar{\nu}_e$ signals from pair annihilation and plasmon decay using models for three stars of 8.4, 12, and $15\,M_{\odot}$, respectively. We plan to carry out a systematic study including more massive stars and taking into account neutrino oscillations in the near future.

ACKNOWLEDGMENTS

We thank Alexander Heger for providing us with models of massive stars. This work was supported in part by the U.S. DOE Grant No. DE-FG02-87ER40328 and by a key laboratory grant (No. 11DZ2260700) from the Office of Science and Technology in Shanghai Municipal Government.

Appendix A: Quantities in the effective squared matrix element

The quantities I_i^B $(i = 1, 2, 3)$ in Eq. (18) for the effective squared matrix element $|\mathcal{M}|^2_{\rm eff}$ are defined as

$$\begin{aligned} I_1^B =& -\frac{2}{\beta_1}(c_1k^2 + 2c_2c_5 - 4c_3c_{12}) + \frac{2}{\beta_2}[4(c_3 - 4c_5)c_9 - c_1k^2 - 2c_2c_5] - \frac{k^2 + 4c_{10}}{\beta_1^2}(c_1c_3 + 8c_6^2) \\ & - \frac{k^2 + 4c_7}{\beta_2^2}[c_1c_3 + 8c_6^2 + 4c_5(2c_5 - c_3)] + \frac{2}{\beta_1\beta_2}\{4c_2c_5^2 + 4c_{11}[c_3(2c_5 - c_1) - 8c_6^2] \\ & + k^2[c_1^2 + 2c_3c_5 + c_1(k^2 - 4m_e^2 - 4c_6 + 2c_7 + 4c_8 + 4c_9 + 2c_{10} - 4c_{12}) \\ & - 8c_6^2 - 8m_e^2(c_8 + c_9 - c_{12})]\} + c_1\left(\frac{\beta_2}{\beta_1} + \frac{\beta_1}{\beta_2}\right) - 8c_8, \end{aligned} \tag{A1}$$

$$\begin{aligned} I_2^B =& -2m_e^2\left\{4c_5\left(\frac{1}{\beta_1} + \frac{1}{\beta_2}\right) + \frac{c_1}{\beta_1^2}(k^2 + 4c_{10}) + \frac{c_1}{\beta_2^2}(k^2 + 4c_7)\right. \\ & \left. -\frac{2}{\beta_1\beta_2}[k^2(c_1 + 4c_8 + 4c_9 - 4c_{12}) + 4c_5^2 - 4c_1c_{11}]\right\}, \end{aligned} \tag{A2}$$

$$\begin{aligned} I_3^B =& -\frac{4c_1(c_4 + 4c_{12})}{\beta_1} + \frac{4c_1}{\beta_2}(c_4 - 4c_9) + \frac{2(k^2 + 4c_{10})c_1c_3}{\beta_1^2} + \frac{2c_1(k^2 + 4c_7)(c_3 - 4c_5)}{\beta_2^2} \\ & + \frac{4c_1}{\beta_1\beta_2}\Big[4(c_3 - 2c_5)c_{11} + k^2(-c_3 + 2c_5 + 2c_7 - 2c_{10} + 4c_9 + 4c_{12})\Big] + 2c_1\left(\frac{\beta_2}{\beta_1} - \frac{\beta_1}{\beta_2}\right), \end{aligned} \tag{A3}$$

where

$$\begin{aligned} & c_1 \equiv P^2 \equiv (p + k - p')^2, \quad c_2 \equiv P^2 - 2m_e^2, \quad c_3 \equiv P^2 + 4p' \cdot q, \\ & c_4 \equiv k^2 + 2k \cdot q, \quad c_5 \equiv k \cdot q, \quad c_6 \equiv p' \cdot q, \\ & c_7 \equiv (p' \cdot \epsilon_B)^2, \ \ c_8 \equiv (q \cdot \epsilon_B)^2, \ \ c_9 \equiv (p' \cdot \epsilon_B)(q \cdot \epsilon_B), \\ & c_{10} \equiv (p \cdot \epsilon_B)^2, \ \ c_{11} \equiv (p \cdot \epsilon_B)(p' \cdot \epsilon_B), \ \ c_{12} \equiv (p \cdot \epsilon_B)(q \cdot \epsilon_B). \end{aligned} \tag{A4}$$

[1] G. Beaudet, V. Petrosian, and E. E. Salpeter, Astrophys. J. **150**, 979 (1967).

[2] D. A. Dicus, Phys. Rev. D **6**, 941 (1972).

[3] P. J. Schinder, D. N. Schramm, P. J. Wiita, S. H. Margolis, and D. L. Tubbs, Astrophys. J. **313**, 531 (1987).

[4] H. Munakata, Y. Kohyama, and N. Itoh, Astrophys. J. **296**, 197 (1985).

[5] Y. Kohyama, N. Itoh, and H. Munakata, Astrophys. J. **310**, 815 (1986).

[6] N. Itoh, T. Adachi, M. Nakagawa, Y. Kohyama, and H. Munakata, Astrophys. J. **339**, 354 (1989).

[7] N. Itoh, H. Mutoh, A. Hikita, and Y. Kohyama, Astrophys. J. **395**, 622 (1992).

[8] Y. Kohyama, N. Itoh, A. Obama, and H. Mutoh, Astrophys. J. **415**, 267 (1993).

[9] Y. Kohyama, N. Itoh, A. Obama, and H. Hayashi, Astrophys. J. **431**, 761 (1994).

[10] N. Itoh, H. Hayashi, A. Nishikawa, and Y. Kohyama, Astrophys. J. Suppl. Ser. **102**, 411 (1996).

[11] N. Itoh, A. Nishikawa, and Y. Kohyama, Astrophys. J. **470**, 1015 (1996).

[12] A. Odrzywolek and A. Heger, Acta Phys. Pol. B **41**, 1611 (2010).

[13] C. Kato, M. D. Azari, S. Yamada, K. Takahashi, H. Umeda, T. Yoshida, and K. Ishidoshiro, Astrophys. J. **808**, 168 (2015).

[14] F. An *et al.*, J. Phys. G **43**, 030401 (2016).

[15] T. Yoshida, K. Takahashi, H. Umeda, and K. Ishidoshiro, Phys. Rev. D **93**, 123012 (2016).

[16] A. Odrzywolek, M. Misiaszek, and M. Kutschera, Astropart. Phys. **21**, 303 (2004).

[17] K. Asakura *et al.* (KamLAND Collaboration), Astrophys. J. **818**, 91 (2016).

[18] L. Wolfenstein, Phys. Rev. D **17**, 2369 (1978).

[19] S. P. Mikheev and A. I. Smirnov, Nuovo Cimento Soc. Ital. Fis. C **9**, 17 (1986).

[20] S. Ratković, S. I. Dutta, and M. Prakash, Phys. Rev. D **67**, 123002 (2003).

[21] S. I. Dutta, S. Ratković, and M. Prakash, Phys. Rev. D **69**, 023005 (2004).

[22] M. Misiaszek, A. Odrzywolek, and M. Kutschera, Phys. Rev. D **74**, 043006 (2006).

[23] A. Odrzywolek, Eur. Phys. J. C **52**, 425 (2007).

[24] K. M. Patton and C. Lunardini, arXiv:1511.02820.

[25] P. Cazzola, G. De Zotti, and A. Saggion, Phys. Rev. D **3**, 1722 (1971).

[26] E. Braaten and D. Segel, Phys. Rev. D **48**, 1478 (1993).

[27] N. Itoh and Y. Kohyama, Astrophys. J. **275**, 858 (1983).

[28] H. Munakata, Y. Kohyama, and N. Itoh, Astrophys. J. **316**, 708 (1987).

[29] N. Itoh, N. Matsumoto, M. Seki, and Y. Kohyama, Astrophys. J. **279**, 413 (1984).

[30] N. Itoh, Y. Kohyama, N. Matsumoto, and M. Seki, Astrophys. J. **285**, 304 (1984).

[31] D. A. Young, E. M. Corey, and H. E. DeWitt, Phys. Rev. A **44**, 6508 (1991).

[32] F. J. Rogers, D. A. Young, H. E. DeWitt, and M. Ross, Phys. Rev. A **28**, 2990 (1983).

[33] S. Ichimaru, H. Iyetomi, S. Mitake, and N. Itoh, Astrophys. J. **265**, L83 (1983).

[34] C. J. Pethick and V. Thorsson, Phys. Rev. D **56**, 7548 (1997).

[35] A. D. Kaminker, C. J. Pethick, A. Y. Potekhin, V. Thorsson, and D. G. Yakovlev, Astron. Astrophys. **343**, 1009 (1999).

[36] N. Itoh, R. Asahara, N. Tomizawa, S. Wanajo, and S. Nozawa, Astrophys. J. **611**, 1041 (2004).

[37] R. F. Sawyer, Phys. Lett. B **630**, 1 (2005).

[38] O. L. Caballero, C. J. Horowitz, and D. K. Berry, Phys. Rev. C **74**, 065801 (2006).

[39] A. Marek, H.-T. Janka, R. Buras, M. Liebendoerfer, and M. Rampp, Astron. Astrophys. **443**, 201 (2005).

[40] T. Hahn, Comput. Phys. Commun. **168**, 78 (2005).

[41] S. E. Woosley, A. Heger, and T. A. Weaver, Rev. Mod. Phys. **74**, 1015 (2002).

[42] A. S. Dighe and A. Y. Smirnov, Phys. Rev. D **62**, 033007 (2000).

[43] A. Odrzywolek, Phys. Rev. C **80**, 045801 (2009).

[44] D. G. Yakovlev, A. D. Kaminker, O. Y. Gnedin, and P. Haensel, Phys. Rep. **354**, 1 (2001).